Linear two-dimensional stability of a Lamb-Oseen dipole as an aircraft wake model

Rémi Jugier, Jérôme Fontane, and Laurent Joly
ISAE-SUPAERO, Université de Toulouse, France

Pierre Brancher
Institut de Mécanique des Fluides de Toulouse (IMFT), Université de Toulouse, CNRS, Toulouse, France

(Received 28 June 2019; published 24 January 2020)

The dynamics of perturbed aircraft wake models is investigated in the two-dimensional limit by means of a linear stability analysis. The base flow, computed by a direct numerical simulation of the incompressible Navier-Stokes equations, is a viscous counter-rotating vortex dipole obtained from an initial condition which is either a superposition of two Lamb-Oseen vortices or a vorticity sheet with elliptical vorticity distribution. The former, referred to as the Lamb-Oseen dipole (LOD), is a model for the far field of the wake and gives rise to a family of quasisteady dipoles parametrized by their aspect ratio only. The later approaches the near-field wake of a wing during the rolling phase which eventually converges towards the LOD model at later times. First, a modal stability analysis of the LOD under the assumption of a frozen base flow is performed for aspect ratios a/b ranging from 0.05 to 0.36 at various Reynolds numbers. Several families of unstable antisymmetric and symmetric modes are observed. The maximal growth rates are reached at low Reynolds numbers. The results are consistent with those obtained by Brion *et al.* [Phys. Fluids **26**, 064103 (2014)] for the higher aspect ratio inviscid Lamb-Chaplygin dipole (LCD). However, the a posteriori verification of the validity of the frozen base flow assumption shows that, except for a few modes occurring at the highest aspect ratios and large Reynolds numbers, these two-dimensional instabilities do not survive the base flow unsteadiness due to viscous diffusion. They are thus not likely to develop in the flow. Second, we focus on the transient dynamics of the dipoles by looking for the optimal perturbations through a nonmodal stability analysis based on a direct-adjoint approach. The observed energy gains are substantial and indicate the potential of transient mechanisms. In the short time dynamics, the optimal perturbation consists of intertwined vorticity layers located within each vortex core and leading to a $m = 2$ deformation Kelvin wave excited by the Orr mechanism. For moderate to large horizon times, the optimal perturbation takes the form of vorticity layers localized outside the vortex core which eventually give rise to the two-dimensional unstable mode unveiled by the modal analysis through a combination of Orr mechanism and velocity induction. The robustness of these modes is examined by considering the initial stage of the development of aircraft wakes. The optimal perturbations developing on an elliptic and a double-elliptic vorticity sheet present a similar structure and rely on the same mechanisms as the ones observed for the LOD but come with lower energy gains. It is concluded that the rolling-up of the vorticity sheet in the near-field of the wake does not influence significantly the linear development of these two-dimensional perturbations.

DOI: 10.1103/PhysRevFluids.5.014701

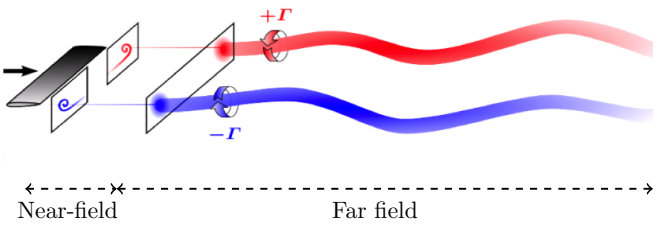

FIG. 1. Sketch of the streamwise development of an aircraft wake. The first sectional plan lies in the near-field region where the vorticity sheet rolls-up. The second one corresponds to the far-field region where the wake takes the form of a counter-rotating vortex dipole. The scales are not representative of real wake.

I. INTRODUCTION

Since the 1960s and the democratization of air transportation, aircraft wake vortices have been the subject of numerous research studies motivated by the associated economic, safety and more recent environmental issues. Invisible in the absence of condensation, the trailing vortices are very hazardous for a follower aircraft due to the intense rolling moment they can induce, requiring the imposition of security standards which limit the takeoff and landing rates in airports, and thereby their capacity and profitability. These vortices also play a role, though not yet completely understood, in the formation and dissemination of condensation trails or "contrails" generated by the aircraft engines. Under specific atmospheric conditions, these contrails lead to the formation of artificial cirrus clouds [1] which affect significantly the local radiative forcing and the photochemistry of the atmosphere. The contribution of aviation to the global radiative forcing is estimated to lie between 3.5% to 4.9% [2]. For all these reasons, the characterization and understanding of the dynamics of these trailing vortices take on an important scientific interest motivated by their control to reduce their lifespan.

Trailing vortices observed in the far field of an aircraft wake result from the roll-up of the vorticity sheet generated at the trailing edge of the wing [3,4] as illustrated in Fig. 1. This initial phase of concentration of the vorticity sheet into two counter-rotating vortices is commonly referred to as the near-field of the wake and extends a few wingspans downstream the trailing edge [4]. An important part of the scientific effort dedicated to the dynamics of aircraft wake has focused on the far field when it has already rolled-up into a vortex dipole, and more specifically on the development of instabilities in the contrails. If an isolated vortex can be subjected to various kinds of instabilities, such as centrifugal [5], trailing [6], viscous [7] or Rayleigh-Taylor [8] ones, then trailing vortices exhibit a dipolar structure and are thus sensitive to three-dimensional instabilities specific to vortex dipoles. Two main types of so-called cooperative instabilities can be observed in real trailing vortices [9]: the Crow instability occurring at long wavelength of the order of the wingspan and the elliptic instability active at shorter wavelength, of the order of the vortex core radius a. Naturally triggered by disturbances and atmospheric turbulence, these instabilities lead to growing 3D distortions on contrails before their reconnection and eventual dissipation after a few minutes. These two instabilities were first predicted theoretically using a vortex filament model, respectively, by Crow [10] and Widnall *et al.* and Moore and Safman [11–13]. Since these pioneering works, the stability of vortex pairs has been extensively studied, like the inviscid Lamb-Chaplygin [14,15] and the viscous Lamb-Oseen [16–18] dipoles, or the stability of a four-vortex model taking into account the wake generated by the horizontal tail of the plane [19,20] (see the recent review of Leweke *et al.* [9] for a complete description).

A new instability has been recently identified by Brion *et al.* [14] in the two-dimensional limit for the Lamb-Chaplygin dipole (LCD) through a modal stability analysis at moderate Reynolds numbers, i.e., $\mathrm{Re} < 3180$. This two-dimensional instability takes the form of two displacement modes located in each vortex core and induces a zigzag displacement of the vortex pair along its unperturbed trajectory associated with viscous mechanisms that are not fully understood. In

the case of the antisymmetric oscillatory mode, the authors point out three different ingredients participating to the dynamics of the unstable mode. First, they note that the instantaneous growth rate of the mode is maximal (respectively, minimal) when the rotating displacement modes located in each vortex core are aligned with the direction of stretching (respectively, compression) induced by the companion vortex. Second, they show that the vorticity of the mode which is leaking outside the Kelvin oval is responsible for the rotation of the perturbation. Finally, they notice that the vorticity of the mode located in the viscous tail of the dipole induces a velocity field inside the dipole with a magnitude comparable to the velocity of the dipole itself, which underlines the important role of the dipole viscous tail in the dynamics of the instability.

Because the LCD presents a discontinuity in its vorticity field at the Kelvin oval boundary, Brion *et al.* [14] also made a single stability calculation for a relatively high aspect ratio Lamb-Oseen dipole (LOD), $a/b = 0.3$, at two Reynolds numbers, and found that the two-dimensional instability observed for the LCD is also present, though with smaller growth rates. They also noted that, at these Reynolds numbers, the characteristic growth time is comparable to the characteristic diffusion time of the dipole, which questions the validity of the modal approach under the assumption of a frozen base flow. Indeed, the vortex dipole evolves under viscous diffusion while being advected downwards at the self-induced velocity $\Gamma/2\pi b$ where Γ and b are, respectively, the vortex circulation and vortex separation. The resulting effect of viscous spreading is twofold: the radius of each vortex increases in time and so does the dipole aspect ratio a/b, and, as a consequence, vorticity progressively diffuses beyond the Kelvin oval generating a viscous tail [21]. The inviscid LCD model does not allow to take into account these combined effects. Besides, its high aspect ratio of the order of $a/b \approx 0.448$ [14] is not representative of real aircraft wake vortices which aspect ratio is smaller, i.e., $a/b \approx 0.1$ [22,23]. These limitations of the LCD model stress the need for a complete stability analysis of a viscous vortex dipole more representative of real aircraft wakes. The present work focuses on the influence of the dipole aspect ratio on this two-dimensional unstable mode.

The choice of the LOD model is motivated by the fact that, in a viscous fluid, most counter-rotating vortex pairs converge, through axisymmetrization and mutual elliptical deformation, towards the same family of dipoles characterized by their aspect ratio only and for which the near Gaussian vorticity distribution obtained on each vortex is very close to the Lamb–Oseen vortex [9,16,21]. Besides, the azimuthal velocity component of a real trailing vortex is correctly represented by the Gaussian profile of the Lamb-Oseen vortex (see the Fig. 4 of Devenport *et al.* [24]). As done previously by Sipp *et al.* [16], Donnadieu *et al.* [18], Delbende and Rossi [21], the LOD is obtained numerically from a direct numerical simulation starting with an initial state consisting of two well-separated counter-rotating Lamb-Oseen vortices. Starting from an initial dipole of very small aspect ratio, i.e., $a/b = 0.025$, which evolves in time under viscous diffusion and self-induced downward advection, we generate a complete family of LODs with aspect ratio up to $a/b = 0.36$. Their characteristics are described in Sec. II together with the numerical method. A great care has been taken to generate the base state, in particular to the compensation of the dipole descent velocity V_d. In Sec. III, this family of LODs provides the base states needed to extend the work of Brion *et al.* [14] and explore the influence of the aspect ratio on the two-dimensional instability. The section ends with an analysis of the effect of the base flow viscous diffusion, neglected in the modal analysis, on the development of these two-dimensional instability modes. Finally, a nonmodal stability analysis is conducted in Sec. IV to investigate the transient growth mechanisms potentially occurring in the LOD. This is a model for the far field and it does not take into account the initial rolling phase of the vorticity sheet generated at the trailing edge of the wing. Hence, the nonmodal analysis, particularly suited to capture short term transient growth, is applied to near-field wake models to ascertain if the linear dynamics is modified by the initial development of the wake. The search for the optimal perturbation is thus conducted for two near-field wake models consisting of elliptical vorticity sheets modeling the cruise or the high-lift takeoff or landing phases.

II. THE LAMB-OSEEN DIPOLE

A. Base flow computation

We consider a two-dimensional viscous flow solution of the incompressible Navier-Stokes equations:

$$\boldsymbol{\nabla} \cdot \mathbf{v} = 0, \tag{1}$$

$$\frac{\partial \mathbf{v}}{\partial t} = \mathbf{v} \times \omega\, \mathbf{e}_z - \boldsymbol{\nabla}\left(p + \frac{\mathbf{v}^2}{2}\right) + \nu \boldsymbol{\Delta} \mathbf{v}, \tag{2}$$

where $\mathbf{v} = (u, v)$, ω, p stand, respectively, for the velocity, vorticity, and pressure fields, and ν is the kinematic viscosity. As done by Sipp *et al.* [16], Donnadieu *et al.* [18], the flow is initialized with a superposition of two counter-rotating axisymmetric Lamb-Oseen vortices of circulation $\Gamma_0 > 0$ and $-\Gamma_0$, dispersion radius a_0 and vortex separation b_0. There are three characteristic time scales associated with the dynamics of the base flow: the characteristic vortex turn-over time $T_a = 2\pi a_0^2/\Gamma_0$, the dipole advection time scale $T_b = 2\pi b_0^2/\Gamma_0$ and the viscous time scale $T_\nu = a_0^2/4\nu$. Unless stated, the results presented in the following will be normalized using T_b. The Reynolds number is classically defined by $\mathrm{Re} = \Gamma_0/\nu$. In the Cartesian coordinate system (x, y) corresponding, respectively, to the horizontal and vertical directions, the vortices are initially located at $(-b_0/2, 0)$ and $(b_0/2, 0)$ so that the corresponding scalar vorticity field is

$$\omega_B(x, y) = -\frac{\Gamma_0}{\pi a_0^2} e^{-[(x+b_0/2)^2+y^2]/a_0^2} + \frac{\Gamma_0}{\pi a_0^2} e^{-[(x-b_0/2)^2+y^2]/a_0^2}. \tag{3}$$

The base flow fields $(\mathbf{v}_B, \omega_B, p_B)$ are obtained by the time integration of Eqs. (1) and (2) from this initial field in a doubly periodic box of size $[-L_x/2, L_x/2] \times [-L_y/2, L_y/2]$ with the same 2D Fourier pseudospectral method used by Donnadieu *et al.* [18], except that temporal integration is done here by a fourth-order Runge-Kutta scheme rather than a second-order Adams-Bashforth scheme. The complete description of the numerical method is already described in details in Donnadieu *et al.* [18], Donnadieu [25], Jugier [26], so we only give here the details associated with the selection of the numerical parameters. The size of the domain is chosen as $L_x \times L_y = 12b_0 \times 16b_0$, which has been checked to be sufficiently large so that the influence of the periodic boundary conditions is negligible; see Jugier [26] for details. The initial aspect ratio of the dipole is set to $a_0/b_0 = 0.025$ and the Reynolds number is equal to $\mathrm{Re} = 2500$. We choose to have at least 10 grid points within each vortex core initially so that the mesh size is 2400×3200.

B. Definition of the relative frame of reference

Due to self-induction, the dipole moves downwards at a speed of approximately $-\Gamma_0/2\pi b_0$. This descent velocity, noted V_d, is compensated so that the dipole is observed to be almost steady in its own frame of reference, only slowly evolving under viscous diffusion. In the previous studies on LOD dynamics [14,16,18,21,27], the definition of the relative frame of reference varies greatly due to the different evaluations of the descent velocity V_d, and its influence on the LOD dynamics has not been addressed carefully so far. We choose here to evaluate the descent velocity V_d as the y component of the velocity at the vortex centers defined by the vorticity extrema, denoted V_1 in the following. But there are four other possible definitions: the Eulerian $V_2 = v_B(x_c, y_c)$ and Lagrangian $V_3 = dy_c/dt$ vertical velocities of the vortex centroid calculated from the first order vorticity momentum $(x_c, y_c) = (\iint_{\mathcal{D}} \omega_B x\, dS, \iint_{\mathcal{D}} \omega_B y\, dS)/\Gamma$ ($\mathcal{D}$ is half of the domain where $x > 0$), the y component of the vorticity-weighted velocity $V_4 = \iint \omega_B v_B\, dS/\Gamma$, and the descent velocity of a pair of point vortices with equivalent circulation and separation distance given by the analytical expression $V_5 = \Gamma/2\pi b$. A good criterion to discriminate the best evaluation of the descent velocity is the minimization of the unsteadiness of the base flow in its own frame of reference. The unsteadiness of the base flow can be assessed from both the velocity and vorticity

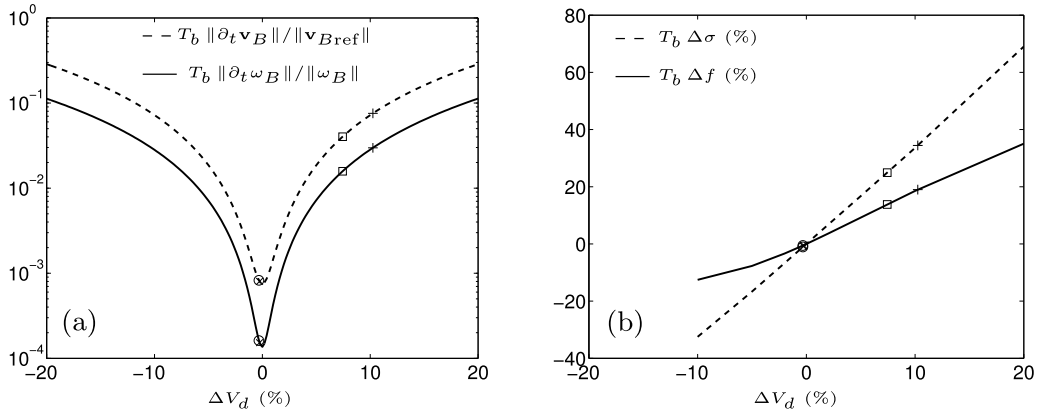

FIG. 2. (a) Measure of the LOD unsteadiness as a function of the descent velocity relative deviation $\Delta V_d = V_d/V_1 - 1$. (b) Influence of ΔV_d on the growth rate and frequency of the antisymmetric mode for $(a/b, \mathrm{Re}) = (0.3, 788)$. The symbols correspond to the different evaluations of the descent velocity: V_2 (+), V_3 (×), V_4 (◯), and V_5 (□).

fields, namely, $T_b \|\partial_t \mathbf{v}_B\|/\|\mathbf{v}_{B\mathrm{ref}}\|$ and $T_b \|\partial_t \omega_B\|/\|\omega_B\|$, where $\|\cdot\|$ stands for the L2-norm defined by Eq. (11) and the velocity field in the absolute frame $\mathbf{v}_{B\mathrm{ref}}$ is used for normalization to avoid any bias in the measure. The unsteadiness of the LOD is measured as a function of the relative deviation ΔV_d of the descent velocity from the definition retained here, namely, the y component of the velocity at the vorticity extrema V_1, i.e., $\Delta V_d = (V_d - V_1)/V_1$. These evolutions are displayed in Fig. 2(a), where it can be observed that none of the different options for the evaluation of V_d leads to a perfectly steady solution. Nevertheless, $V_d = V_1$ is the best choice since it gives the minimum of base flow unsteadiness. Evaluations of the descent velocity by V_3 and V_4 are also good candidates since they are very close to that minimum, but they were discarded anyway since V_1 is much easier to compute. A correct evaluation of the descent velocity is crucial when considering the modal stability analysis of the dipole since the characteristics of the unstable modes are seen to be sensitive to the compensation of V_d from Fig. 2(b). For the most amplified antisymmetric mode obtained for $(a/b, \mathrm{Re}) = (0.3, 788)$, the relative deviations on the growth rate are as large as 30%.

C. Characterization of the base flow

As discussed by Sipp *et al.* [16] and Delbende and Rossi [21], the computation of the base flow from the initial conditions Eq. (3) starts with a short transient regime during which the two counter-rotating circular vortices adapt to the strain field imposed by their counterpart and become elliptical. This transient adaptation phase is characterized by oscillations occurring in the vortex core and takes the form of an elliptical rotating mode of period $4\pi T_a$. These oscillations are damped within a few T_a.

After the initial transient adaptation, the vortex dipole evolves slowly under viscous diffusion towards larger aspect ratios. Figure 3 illustrates the evolution of the vorticity field ω_B and the streamlines of the LOD in its frame of reference for increasing aspect ratios. A specific family of logarithmic-linear hybrid scales has been adopted here for the representation of the vorticity contours to emphasize the viscous tail in the wake of the dipole:

$$\mathrm{E}_n = \{\pm M 10^{-n+i/3},\, i \in [0, 3(n-1)]\} \cup \{\pm iM/10,\, i \in [2, 10]\}, \tag{4}$$

where M stands for the maximal absolute value of the plotted quantity and n is a positive integer. As already described by Delbende and Rossi [21], the viscous evolution of the LOD is divided in two phases. For small values of a/b, the two vortices remain separated so that their respective vorticity

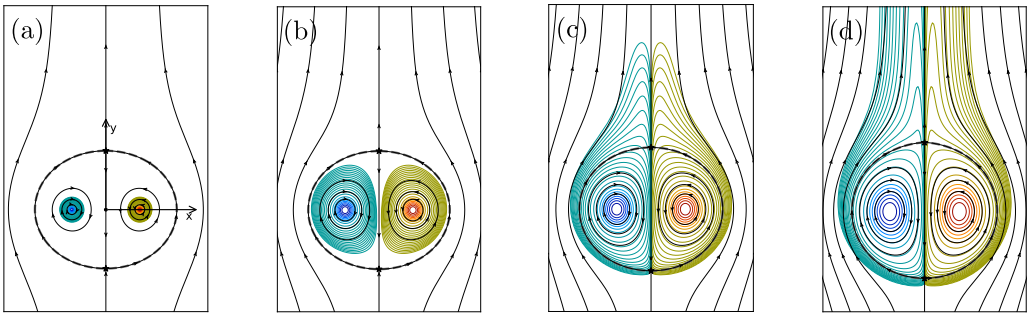

FIG. 3. Streamlines (black solid lines) and vorticity contours (color scale E_6, see Eq. (4) and text for details) for four LODs of increasing aspect ratio: (a) $a/b = 0.05$, (b) $a/b = 0.15$, (c) $a/b = 0.25$, and (d) $a/b = 0.35$. A small part of the computational domain is represented, i.e., $(x, y) \in [-1.5b, 1.5b] \times [-1.5b, 3b]$. The dotted thick line corresponds to the Kelvin oval.

fields do not overlap. The circulation $\Gamma = \iint_{\mathcal{D}} \omega_B \, dx \, dy$ of each vortex is constant and the symmetry of the dipole with respect to the x-axis is preserved. In the second phase, vorticity diffusion across the separatrix between the two vortices yields a decrease of the circulation. Besides, due to vorticity diffusion across the Kelvin oval, a viscous tail forms in the dipole wake and breaks off its symmetry with respect to the x axis. As mentioned in the Introduction, the evolution of the base flow after the initial transient gives rise to a family of dipoles characterized by their aspect ratio only [16,21]. This is corroborated here by following the evolution of the dipole characteristics with its aspect ratio a/b for four values of the initial Reynolds number $\mathrm{Re} = 2\,500$, $5\,000$, $7\,500$, and $10\,000$. We first consider the ellipticity of the vortices, defined as the ratio a_y/a_x of the vortex core radii along the y and x directions calculated from the second-order moments of vorticity:

$$a_y = \sqrt{\frac{1}{\Gamma} \iint_{\mathcal{D}} \omega_B (y - y_c)^2 \, dx \, dy} \quad \text{and} \quad a_x = \sqrt{\frac{1}{\Gamma} \iint_{\mathcal{D}} \omega_B (x - x_c)^2 \, dx \, dy}. \tag{5}$$

Figure 4(a) shows that the ellipticity evolution does depend on a/b and that the influence of the Reynolds number is negligible. Figure 4(b) shows the evolution of the total circulation Γ and the inner circulation Γ_i obtained by integration of the vorticity field over the area delimited by the Kelvin oval, i.e., rejecting the contribution of the viscous tail. It can be seen that for aspect ratios below $a/b \approx 0.3$, all curves are superimposed. This result implies that the circulation decay only

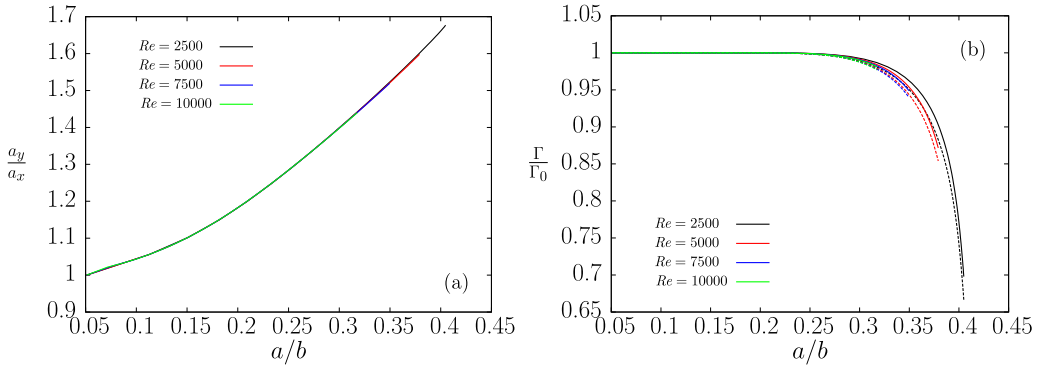

FIG. 4. Evolution of (a) ellipticity a_y/a_x and (b) circulations $\frac{\Gamma}{\Gamma_0}$ (solid lines), $\frac{\Gamma_i}{\Gamma_0}$ (dotted lines) of the vortices as a function of the dipole aspect ratio a/b for various Reynolds numbers.

depends on the aspect ratio of the dipole. The viscous effects become significant for larger aspect ratios with the substantial contribution of the viscous tail to the total circulation, which amount is driven by the Reynolds number. The decrease of the circulation given by the ratio Γ/Γ_0 measured for $\mathrm{Re} = 5000$ differs from the one measured for $\mathrm{Re} = 2500$ by about 1% when the dipole aspect ratio is $a/b = 0.36$. We thus consider that the LOD is no longer Reynolds independent beyond this value. Besides, the initial adaptation phase, which lasts few T_a, has already ended when the dipole aspect ratio reaches the value of $a/b = 0.05$ by $t \sim 4500T_a$. Thus only the base flows obtained for $0.05 \leqslant a/b \leqslant 0.36$ and $\mathrm{Re} = 2500$ will be used for the modal stability analysis in the next section.

III. LINEAR MODAL STABILITY ANALYSIS OF THE LOD

A. Numerical method

The Navier-Stokes Eqs. (1) and (2) are linearized around a frozen base state $[\mathbf{v}_B, \omega_B, p_B]$ computed by the procedure described in Sec. II A and corresponding to a chosen aspect ratio a/b. The linearization yields the following equations for a small 2D perturbation $[\mathbf{v}, \omega, p]$:

$$\boldsymbol{\nabla} \cdot \mathbf{v} = 0, \tag{6}$$

$$\frac{\partial \mathbf{v}}{\partial t} = \mathbf{v}_B \times \omega\, \mathbf{e}_z + \mathbf{v} \times \omega_B\, \mathbf{e}_z - \boldsymbol{\nabla}(p + \mathbf{v}_B \cdot \mathbf{v}) + \nu \boldsymbol{\Delta} \mathbf{v}. \tag{7}$$

These equations are advanced in time from an initial divergence-free white noise with the same pseudospectral method used for the generation of the base flow. The constraint to have at least 10 grid points within each vortex core is maintained so the mesh size is adapted to the aspect ratio of the LOD: 2400×3200 for $a/b \in [0.05, 0.12]$, 1200×1600 for $a/b \in [0.13, 0.2]$, and 600×800 for $a/b \in [0.21, 0.36]$. The temporal integration is made over a sufficiently long period so that the 2D perturbation fields have converged toward the most amplified mode. Since the coefficients of this linear PDE system are time independent, in the long-term asymptotic limit, the solution is of the form

$$\mathbf{v}(x, y, t) = \Re\{\hat{\mathbf{v}}(x, y) e^{i\omega t}\} = [\mathbf{v}_r \cos(2\pi f t) - \mathbf{v}_i \sin(2\pi f t)] e^{\sigma t}, \tag{8}$$

with $\hat{\mathbf{v}} = \mathbf{v}_r + i\mathbf{v}_i$ and $\omega = 2\pi f - i\sigma$ where f and σ stand, respectively, for the frequency and the growth rate of the mode. For stationary modes, i.e., $f = 0$, the spatial structure is steady and reduces to $\mathbf{v}_r$, and its energy grows exponentially. For oscillatory modes, i.e., $f \neq 0$, the fields $\mathbf{v}_r$ and $\mathbf{v}_i$ can be chosen uniquely on a period so that $\langle \mathbf{v}_r, \mathbf{v}_i \rangle = 0$ and $\|\mathbf{v}_r\|^2 + \|\mathbf{v}_i\|^2 = 1$ with $\|\mathbf{v}_r\| \geqslant \|\mathbf{v}_i\|$, where the scalar product $\langle , \rangle$ and its associated norm are defined by Eq. (11) in the next section. The energy presents oscillations of the form

$$E(t) = \frac{\|\mathbf{v}_r\|^2 + \|\mathbf{v}_i\|^2}{4} [1 + \alpha \cos(4\pi f t)] e^{2\sigma t}, \tag{9}$$

where $\alpha = \frac{\|\mathbf{v}_r\|^2 - \|\mathbf{v}_i\|^2}{\|\mathbf{v}_r\|^2 + \|\mathbf{v}_i\|^2} < 1$ is a nondimensional coefficient that represents the amplitude of these oscillations. When $\alpha \to 0$, the spatial structure of the mode transitions smoothly over the period from $\mathbf{v}_r \to -\mathbf{v}_i \to -\mathbf{v}_r \to \mathbf{v}_i$ and back to $\mathbf{v}_r$, while when $\alpha \to 1$, the spatial structure of the mode is mostly given by $\pm\mathbf{v}_r$ over the period except for rapid transitions to $\mp\mathbf{v}_i$ around $ft = 0.25 + 0.5n$ with $n \in \mathbb{Z}$. Finally, the base state being symmetric, the linearized Navier-Stokes Eqs. (1) and (2) preserve symmetry and it is thus possible to compute separately the most amplified antisymmetric and symmetric modes, as it is usually the case for dipole stability studies.

B. Antisymmetric modes

We now consider the most unstable antisymmetric mode which develops on the frozen base flow described in the previous section as a function of the LOD aspect ratio for six values of the Reynolds number, i.e., $\mathrm{Re} \in \{223, 350, 500, 1280, 2500, 5000\}$. Cases $\mathrm{Re} = 223$ and $\mathrm{Re} = 1280$

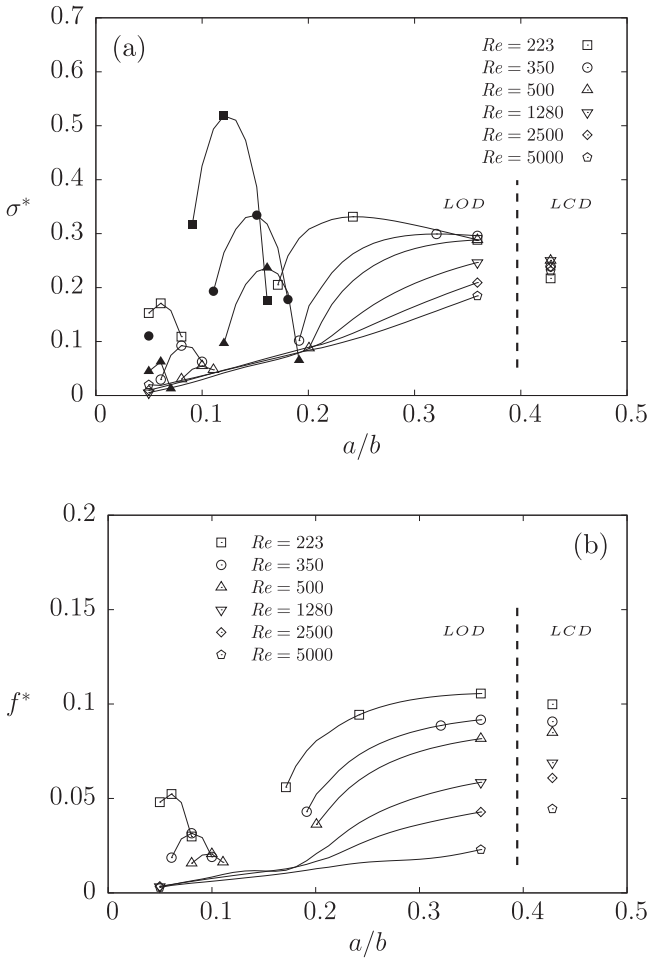

FIG. 5. Nondimensional growth rate σ^* (a) and frequency f^* (b) of the most amplified antisymmetric mode as a function of the dipole aspect ratio a/b for different Reynolds numbers. Oscillatory and stationary branches are, respectively, identified by the hollow and filled symbols positioned at the extremities and maximum of each branch. Growth rates and frequencies for the LCD computed by Brion *et al.* [14] are added for comparison.

are selected to allow comparison with the results of Brion *et al.* [14] obtained for the LOD. The normalized growth rates $\sigma^* = T_b\sigma$ and frequencies $f^* = T_b f$ of these modes are shown in Fig. 5. For large Reynolds numbers, i.e., Re $\geqslant$ 1280, the most amplified mode is oscillatory and both its growth rate and frequency are increasing monotonously with the dipole aspect ratio, with nearly zero growth rate for the smallest aspect ratio. This suggests that the unstable mode disappears in the limit of infinite Reynolds number and zero aspect ratio, a result which is consistent with the absence of such two-dimensional instability in the inviscid analysis performed by Crow [10] for a pair of vortex filaments. For smaller Reynolds numbers, the picture drastically changes: as the dipole aspect ratio decreases, multiple unstable branches of oscillatory and stationary modes are observed with a maximum amplification of each branch corresponding to a specific value of a/b. Surprisingly, each branch exhibits larger growth rates when the Reynolds number decreases. This destabilizing effect of viscosity is unusual since it is generally expected that decreasing the Reynolds number results in the damping of the unstable modes. In the case of the LCD, Brion *et al.* [14] observed a similar trend

when decreasing Reynolds number but the growth rate eventually reaches a maximum before the mode becomes stable below a critical value of $\mathrm{Re}_c = 75$ [28]. This must be also the case for the LOD since the linearized Navier-Stokes equations in the limit of zero Reynolds number show that these 2D modes must vanish. This is readily observable for both stationary modes with $a/b \in [0.16, 0.17]$ and oscillatory ones with $a/b \in [0.34, 0.36]$ where the value of the growth rates are smaller for $\mathrm{Re} = 223$ than for $\mathrm{Re} = 350$. In these figures, the results obtained by Brion *et al.* [14] for the LCD are also reported for $a/b \approx 0.4297$ [29], using our normalization based on Γ and b instead of using the descent velocity V_d of the dipole and the diameter D of the Kelvin oval as characteristic scales ($D \approx 2.174b$ and $V_d \approx 0.135\Gamma/b$). Extrapolation of the different branches obtained for the LOD towards larger aspect ratios seems to be in fair agreement with the values obtained by Brion *et al.* [14] for the LCD. It suggests that the differences of internal structure between the two dipoles do not have a significant impact on the development of these 2D modes, a conclusion which was hinted by Brion *et al.* [14]. As a test case in their Appendix A, they made one stability calculation for the LOD for $a/b = 0.3$ and $\mathrm{Re} = 223$. However, it should be noted that the characteristics of the mode they determined for this specific case do not match the present results, most probably because they used V_2 to evaluate the descent velocity of the dipole, which we proved to have a strong impact on the stability calculations (see Sec. II B).

The vorticity field of these unstable modes is displayed in Fig. 6 for four different values of $(a/b, \mathrm{Re})$ corresponding to oscillatory modes. The vorticity is mostly concentrated into two symmetric displacement modes [30] located in each vortex core of the LOD with some additional residual vorticity spreading in the viscous tail of the dipole. The orientation of the perturbation in the vortex cores changes in time along with the projection of the mode on its real and imaginary part, according to Eq. (8). It results in a full rotation of the mode over a period which can be assessed in Fig. 7(b) by the evolution of the angle θ between the x-axis and the line connecting the two vorticity extrema of one of the displacement mode, as illustrated in Fig. 7(a). It can be seen that the rotation rate is not uniform along the period and depends on the value of the coefficient α as defined in Eq. (9). For $a/b = 0.24$ and $\mathrm{Re} = 223$, α is small and the structure of the mode transitions smoothly between its real and imaginary parts. The rotation is almost regular throughout the period. However, for the same aspect ratio but at larger Reynolds numbers, i.e., $\mathrm{Re} = 1280$ and $\mathrm{Re} = 2500$, the coefficient α is close to unity and therefore the mode remains projected on its real part most of the period except for two very short intervals around $ft = 0.25$ and $ft = 0.75$ where its structure is collinear to its imaginary part. This yields a fast rotation at these two instants while the angle θ is almost constant during the rest of the period. These unevenly rotating displacement modes induce a periodic zigzag motion of the LOD around its unperturbed downward straight trajectory [14]. Comparison between the two first columns of Fig. 6 points out the effect of the dipole aspect ratio on the mode structure. When a/b is small, the displacement modes extend towards the Kelvin oval into spiraling arms of vorticity that are not present for larger aspect ratios. A decrease of the aspect ratio also induces a sharper and more irregular rotation of the mode associated with the increase of the coefficient α, see the case corresponding to $a/b = 0.06$ in Fig. 7(b). The modifications of the mode associated with the increase of the Reynolds number are also twofold. First, the extension of the vorticity field in the viscous tail of the dipole reduces in width as seen in Fig. 6. Second, the coefficient α increases towards unity which implies a more abrupt rotation of the mode. Finally, it should be mentioned that the structure and the kinematics of the stationary modes (not shown) are similar to those of the oscillatory ones except that the real and imaginary parts of the vorticity field are equal.

C. Symmetric modes

The picture is quite similar for the symmetric unstable modes which normalized growth rate σ^* and frequency f^* are displayed in Fig. 8 for the same Reynolds numbers. A notable difference with the antisymmetric case is that most of the modes are stationary. For Reynolds numbers larger than 1280, there is only one branch of stationary instability with moderate to low growth rates.

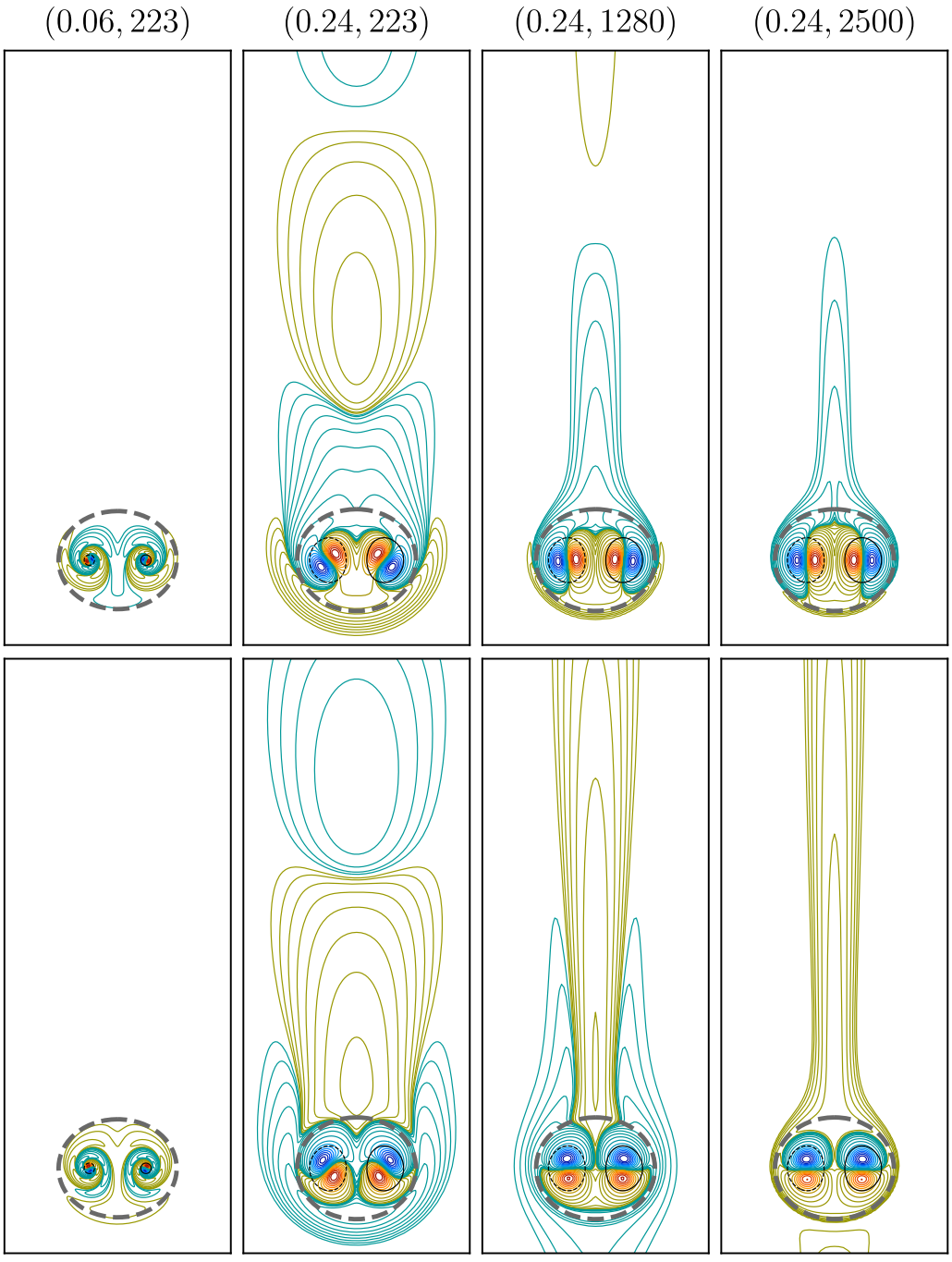

FIG. 6. Real (top) and imaginary (bottom) parts of the vorticity field of antisymmetric oscillatory unstable modes for various values of $(a/b, \mathrm{Re})$ indicated above the figures. From left to right, $\alpha = 0.931, 0.621, 0.971,$ and 0.987. A small part of the computational domain is represented, i.e., $(x, y) \in [-2b, 2b] \times [-1.5b, 10b]$. The E_4 scale is used. The dotted thick line corresponds to the Kelvin oval while the solid and dotted thin lines correspond to $\omega_B = \pm 0.1 \|\omega_B\|_\infty$.

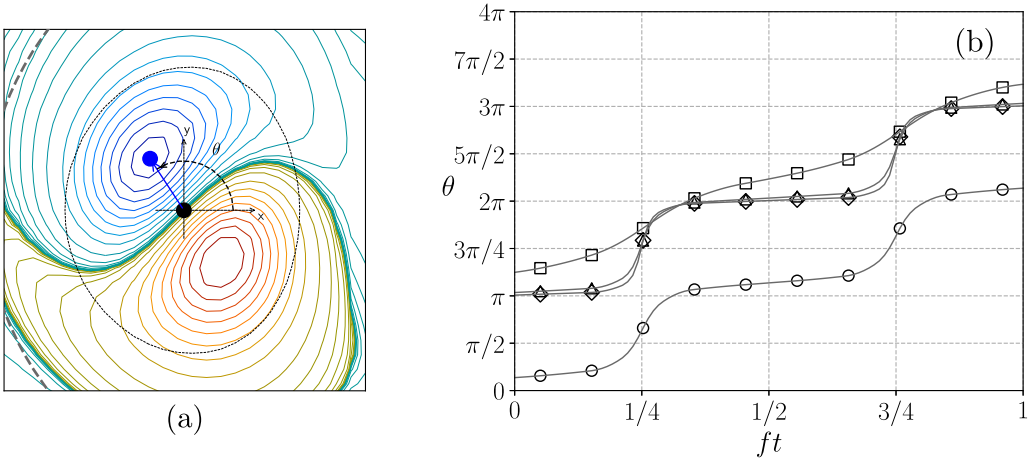

FIG. 7. (a) Definition of the orientation angle θ on a close-up view (left vortex) of the unstable mode obtained for $(a/b, \mathrm{Re}) = (0.24, 223)$. (b) Evolution over one period of θ for antisymmetric modes presented in Fig. 6: $(a/b, \mathrm{Re}) = (0.06, 223)$ (◯), $(a/b, \mathrm{Re}) = (0.24, 223)$ (□), $(a/b, \mathrm{Re}) = (0.24, 1280)$ (△), and $(a/b, \mathrm{Re}) = (0.24, 2500)$ (◇).

Below this value, there are successive branches of stationary and oscillatory instabilities with much larger growth rates, up to $\sigma^* = 0.65$ for $(a/b, \mathrm{Re}) = (0.17, 223)$. As for the antisymmetric modes, these instabilities must vanish in the limit of zero Reynolds number, which implies that, for a given aspect ratio, the growth rate reaches a maximum before decreasing when the Reynolds number is lowered. This Reynolds number of maximum growth rate has not been reached here and must be smaller than $\mathrm{Re} = 223$ for most of the aspect ratios explored, except for $a/b \geqslant 0.3$ where it lies between $\mathrm{Re} = 223$ and $\mathrm{Re} = 350$. For the LCD, Brion *et al.* [14] found a value of $\mathrm{Re} = 4983$ which is much larger. The growth rates corresponding to the modes of the LCD have also been added for $a/b = 0.4297$ and they seem to be in good agreement with our results when the curves obtained for the LOD are extrapolated towards larger aspect ratios. As for the antisymmetric modes, the calculation performed by Brion *et al.* [14] for the LOD with $(a/b, \mathrm{Re}) = (0.3, 1280)$ does not match the present results and has not been reported in Fig. 8. This discrepancy is again very likely due to the way the dipole descent velocity is calculated.

Figure 9 shows the vorticity fields of these stationary symmetric modes for four different values of $(a/b, \mathrm{Re})$. They consist of two antisymmetric displacement modes located at each vortex core which induce a symmetric translation of the two vortices. The influence of both the aspect ratio and the Reynolds number on the structure of these modes is identical to what has been observed for the antisymmetric modes. Spiraling arms of vorticity are present for small aspect ratios and the vorticity extending in the viscous tail of the dipole is thinner when the Reynolds number is increased.

D. Damping due to base flow diffusion

The frozen base flow hypothesis used for the modal approach must be validated a posteriori by comparing the growth rate of the unstable modes with the characteristic time of the base flow evolution which is given by the viscous time scale $T_\nu = a_0^2/4\nu$. For the frozen base flow approximation to be valid, one must ensure that $\sigma T_\nu \gg 1$. We recall that the time evolution of the dispersion radius of a viscous vortex is given by $a^2(t) = a_0^2 + 4\nu t$. The dispersion radius thus increases by about 40% over one T_ν unit. As already pointed out by Brion *et al.* [14], the present two-dimensional instabilities, which exhibit particularly strong growth rates at low Reynolds numbers, might be counteracted by the base flow diffusion. This is confirmed in Fig. 10 where the growth rates have been normalized by T_ν. Only the antisymmetric modes occurring at large aspect

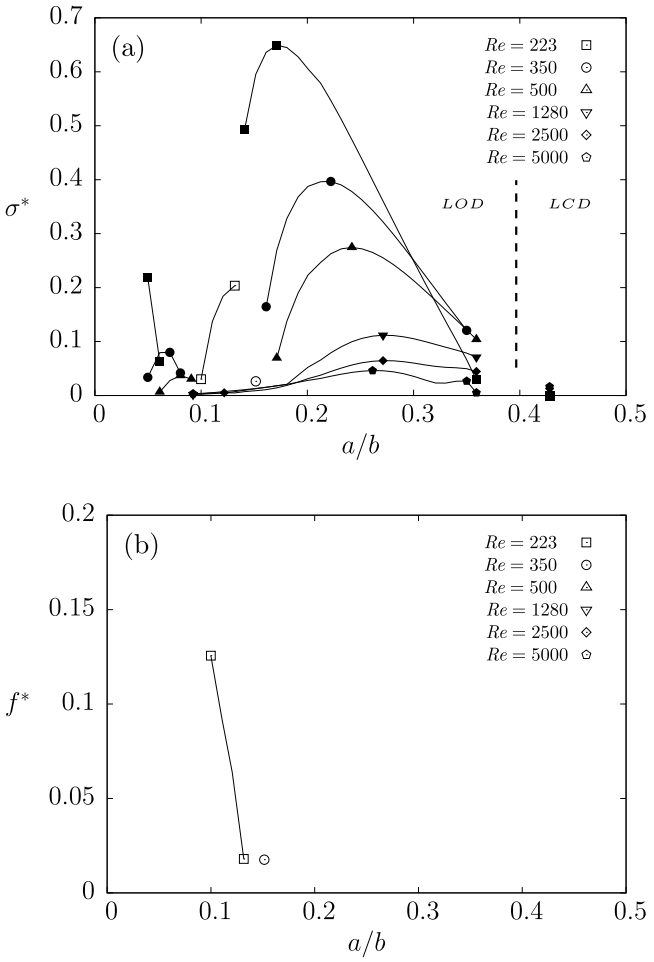

FIG. 8. (a) Growth rates σ^* and (b) frequencies f^* of the most amplified symmetric mode as a function of the dipole aspect ratio a/b for different Reynolds numbers. Same conventions as described in the caption of Fig. 5.

ratios and large Reynolds numbers might be able to develop upon the time dependent base flow since they grow somewhat faster than the diffusion of the dipole (the largest value being $T_\nu\sigma \approx 5$). We have performed a direct numerical simulation of the linearized Navier-Stokes Eqs. (6) and (7) initialized by an unstable mode, in which the base flow was allowed to evolve in time under viscous diffusion. Two modes were considered: the oscillatory antisymmetric and the stationary symmetric modes for $a/b = 0.25$ and $\mathrm{Re} = 5000$ for which $T_\nu\sigma$ is 1.35 and 5.55, respectively. The linear evolution of the oscillatory mode can be initialized with the perturbation taken at any instant within the oscillating period. Three different initial conditions have been tested according to Eq. (9) for the evolution of the perturbation energy $E(t)$: the mode taken at the instants t_M and t_m corresponding, respectively, to the local maximum and the local minimum of the perturbation energy over a given period, as well as at an intermediate time $t_{\mathrm{med}} = \frac{t_{m_1}+t_{m_2}}{2}$ corresponding to the mean time between two consecutive local minima of energy. The corresponding energy gain evolutions are displayed in Fig. 11 along with the ones obtained for a frozen base flow. As expected, if the diffusion of the base flow does not alter significantly the growth of the antisymmetric mode, it quickly stops the development of the symmetric one. When the antisymmetric mode is initialized at

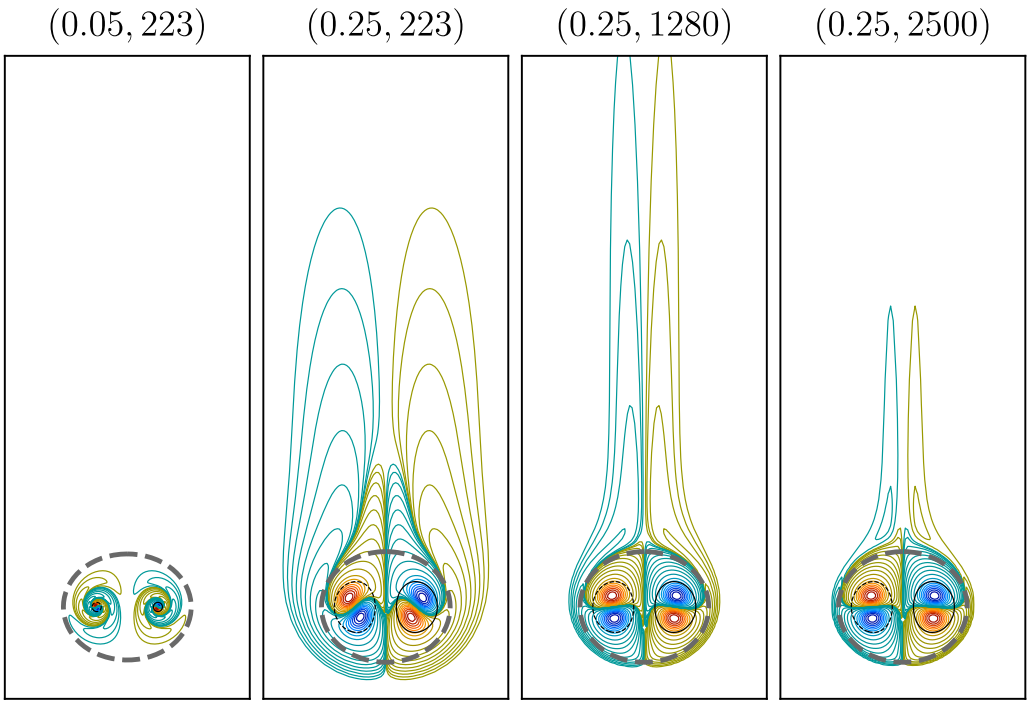

FIG. 9. Vorticity field of symmetric stationary modes for various values of $(a/b, \mathrm{Re})$ indicated above the figures. Same conventions as described in the caption of Fig. 6.

t_m, it benefits from the instantaneous positive growth rate and its energy increases while its energy decreases if initialized at t_M where the instantaneous growth rate turns negative. When initialized at t_{med}, the evolution of the energy lies in between, exhibiting a weaker growth. Other simulations (not presented here) have been conducted for smaller aspect ratios and smaller Reynolds numbers [26] and the conclusion remains unchanged: the base flow diffusion prevents the growth of these two-dimensional modes.

IV. LINEAR NONMODAL STABILITY ANALYSIS OF THE LOD

Since most of the previously identified two-dimensional modes do not grow fast enough when the base flow is submitted to viscous diffusion, we now examine the transient linear dynamics by looking at the optimal perturbation maximizing the energy gain over a given interval of time $[0, T_f]$. We first consider the LOD which corresponds to the far field of an aircraft wake. Then we turn towards the near-field wake with a base flow taken as a vorticity sheet rolling up into a counter-rotating vortex dipole.

A. Numerical method

The nonmodal stability analysis focuses on the 2D transient dynamics of perturbed aircraft wakes models by computing the optimal perturbation over a given time interval $[0, T_f]$. The optimal perturbation is classically defined as the initial condition maximizing the energy gain over the considered time interval:

$$G(T_f) = \frac{E(T_f)}{E_0}, \tag{10}$$

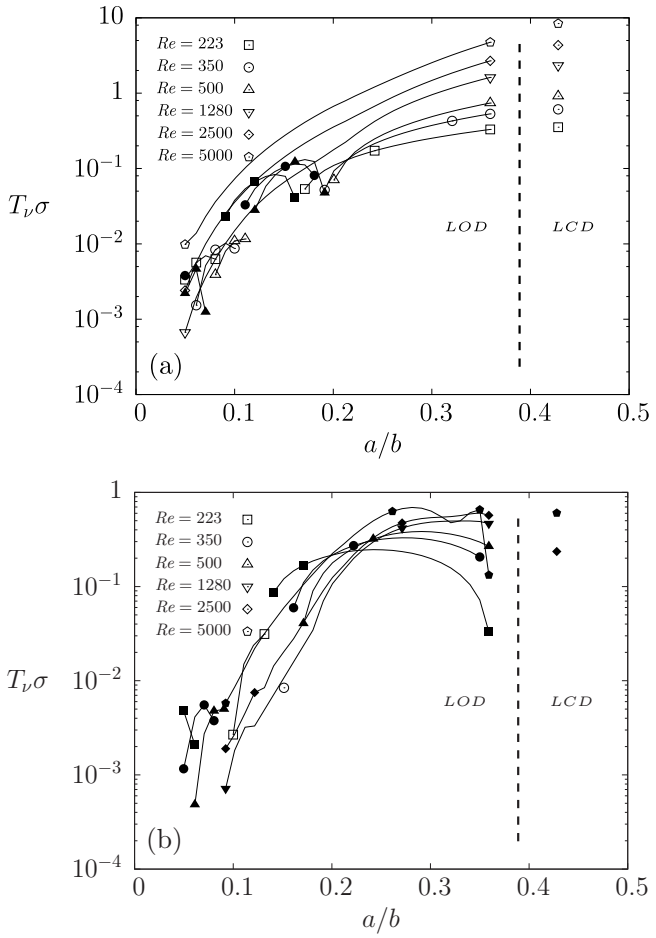

FIG. 10. Growth rates $T_v\sigma$ normalized by the dipole viscous time scale for both (a) antisymmetric and (b) symmetric two-dimensional modes as a function of a/b for different Re. Same conventions as described in the caption of Fig. 5.

where E_0 stands for the initial kinetic energy of the perturbation. The energy definition is associated with the scalar product $\langle , \rangle$ calculated over the computational domain:

$$E(t) = \langle \mathbf{v}, \mathbf{v} \rangle = \|\mathbf{v}\|^2 = \int_{-L_x/2}^{L_x/2} \int_{-L_y/2}^{L_y/2} \mathbf{v}^* \cdot \mathbf{v}\, dx\, dy. \tag{11}$$

Here the superscript * denotes the conjugate transpose. This optimization problem is solved within the framework of the optimal control theory. Constraints are imposed to the perturbation: its initial amplitude is fixed to some constant, i.e., $\|\mathbf{v}(0)\| = v_c$ and the perturbation must be a solution of the linearized Navier-Stokes Eqs. (6) and (7). This can be transformed into an optimization problem without constraint using the variational method of the Lagrange multipliers [31]. The optimal solution is determined by use of the gradient descent, which in turn requires the solving of the so-called linearized Navier-Stokes adjoint equations [18,31]:

$$\nabla \cdot \mathbf{v}^+ = 0, \tag{12}$$

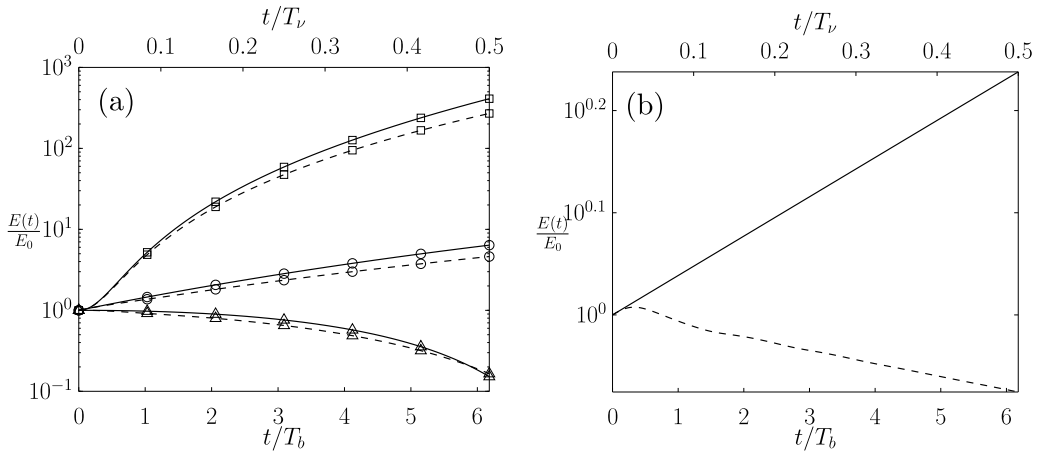

FIG. 11. Energy gain evolution of (a) the antisymmetric oscillatory mode and (b) the symmetric stationary mode for $(a/b, \mathrm{Re}) = (0.25, 5000)$, for a frozen (solid line) and a time-evolving (dashed line) base flow. The oscillatory mode is initialized at three different instants within the period: t_m (□), t_{med} (◯), and t_M (△).

$$-\frac{\partial \mathbf{v}^+}{\partial t} = \omega_B\, \mathbf{e}_z \times \mathbf{v}^+ - \boldsymbol{\nabla} \times (\mathbf{v}_B \times \mathbf{v}^+) - \boldsymbol{\nabla} p^+ + \nu \boldsymbol{\Delta} \mathbf{v}^+. \tag{13}$$

These equations are solved backward in time from $t = T_f$ to $t = 0$, as indicated by the minus sign in front of the time derivative in Eq. (13), using the same pseudospectral method as for the generation of the base flow. The complete description of the optimization algorithm is provided in Ref. [26]. We only give here the main lines:

(1) The velocity field $\mathbf{v}$ is initialized with a white noise with the condition $\|\mathbf{v}(0)\| = v_c$ ($v_c = 1$ for instance).

(2) The direct linearized Navier-Stokes Eqs. (6) and (7) are advanced in time up to the horizon time T_f.

(3) The initial condition for the adjoint equations is computed from the terminal condition $\mathbf{v}^+(T_f) = 2\,\mathbf{v}(T_f)/E_0$.

(4) The adjoint linearized Navier-Stokes Eqs. (12) and (13) are integrated backward in time from $t = T_f$ to $t = 0$.

(5) A new initial condition for the direct equations is obtained from the optimality condition $\mathbf{v}(0) = E(T_f)\mathbf{v}^+(T_f)/2E_0^2$ before going back to step 2.

This optimization loop is stopped when the convergence is reached in terms of the optimal energy gain, namely, $|G^{n+1}(T_f) - G^n(T_f)|/G^n(T_f) < 10^{-2}$.

B. Transient growth on a far-field LOD

As mentioned in Sec. II C, there are three possible time scales that can be used to characterize the dynamics of the LOD, namely, T_a, T_b, and T_ν. Given the values of the aspect ratios and Reynolds numbers considered here, T_a is the smallest time scale since $T_a/T_b = (a_0/b_0)^2 \ll 1$ and $T_a/T_\nu = 8\pi/\mathrm{Re} \ll 1$. Therefore, we chose to observe the short time dynamics of the LOD in number of vortex core rotations, namely, $2\pi T_a$. We consider the optimal perturbation developing over a time-evolving LOD of initial aspect ratio $a_0/b_0 = 0.15$ for three horizon times corresponding to 1, 10, and 60 vortex core rotations: $T_f = 2\pi T_a \approx 0.15 T_b$, $T_f = 20\pi T_a \approx 1.5 T_b$, and $T_f = 120\pi T_a \approx 9 T_b$. Figure 12 presents the energy gain evolution of these optimal perturbations for both the antisymmetric and symmetric cases and for three different Reynolds numbers. The levels of amplification observed are substantial and both modes exhibit similar energy gains except for

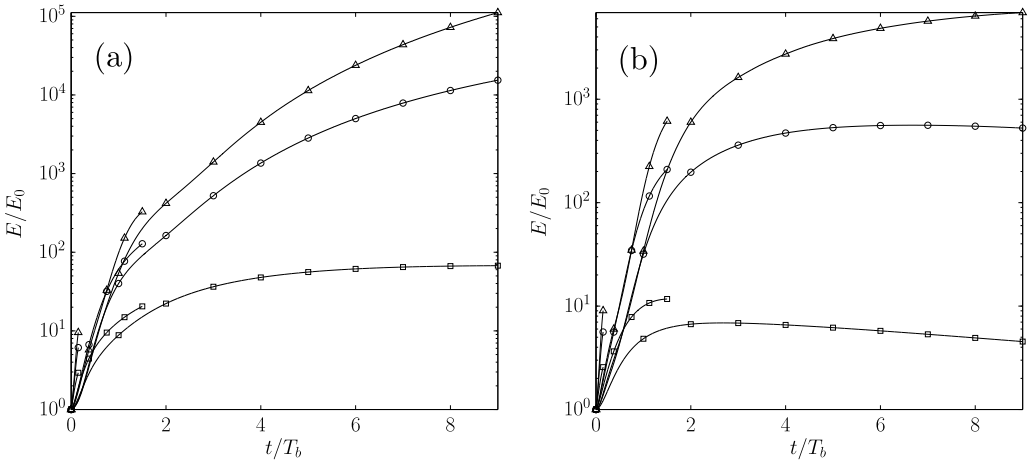

FIG. 12. Time evolution of the energy gain of the (a) antisymmetric and (b) symmetric optimal perturbations obtained for a LOD of aspect ratio $a_0/b_0 = 0.15$ for three horizon times, $T_f/T_b \in \{0.15, 1.5, 9\}$, and three Reynolds numbers, Re $= 223$ (□), Re $= 1280$ (◯), and Re $= 5000$ (△).

the large horizon time where the energy gains of the antisymmetric perturbation are one order of magnitude higher than the symmetric ones. As the horizon time is increased, the mean growth rate $\frac{\log G(T_f)}{2T_f}$ decreases which indicates that the most efficient mechanisms of energy growth are active in the short time dynamics. For the largest horizon time $T_f = 9T_b$, a drop in the energy growth is even observed around $t \approx 2T_b$ and it is more pronounced for the symmetric perturbations. In contrast with the modal analysis, the influence of the Reynolds number is here standard, with a decrease of the optimal energy gain with the diminution of the Reynolds number. The energy gains obtained here for $(a/b, \text{Re}) = (0.15, 1280)$ are in good agreement with those computed recently by Navrose *et al.* [32] for a LOD with $(a/b, \text{Re}) = (0.18, 1000)$ [see their Fig. 18(a)].

The vorticity field of both the optimal perturbations ω_0 and the optimal outcomes ω_f are displayed in Fig. 13 for Re $= 1280$ and the three horizon times investigated. The fields corresponding to the short time dynamics, $T_f = 0.15T_b$, are noticeably different from those obtained for medium to large horizon times. In the first case, the optimal perturbation consists of intertwined thin vorticity layers with a double helix periodicity located inside each vortex core. They progressively uncoil under the differential base flow rotation to give rise to the optimal response under the form of a $m = 2$ deformation mode inside each vortex core [30]. Even if the final state at $t = T_f$ is similar to the one obtained for an isolated Lamb-Oseen vortex [33,34], the physical mechanism responsible for the energy growth relies here solely on the classical Orr mechanism; there is no core-contamination induced by a resonance because the vorticity layers are here located within the vortex core. Once uncoiled, the initial vorticity layers concentrate directly into a $m = 2$ deformation mode of the vortex cores.

For larger horizon times, the initial perturbation is localized outside the vortex core and takes also the form of vorticity layers which are mainly localized along the contracting manifold of the trailing (respectively, leading) hyperbolic stagnation point for the antisymmetric (respectively, symmetric) case. These perturbations are very similar to those observed by Donnadieu *et al.* [18], Brion *et al.* [35] for the three-dimensional optimal perturbations leading at large time to the Crow instability. These optimal perturbations ultimately lead to a response which is similar to the modes identified in the previous section and consists of a $m = 1$ displacement mode located within each vortex core. The associated mechanism of energy growth is here slightly different from the one unveiled by Brion *et al.* [35] for the Crow instability since vortex-stretching is not active here in this two-dimensional flow. The initial growth relies again on the Orr mechanism which is then taken over by a

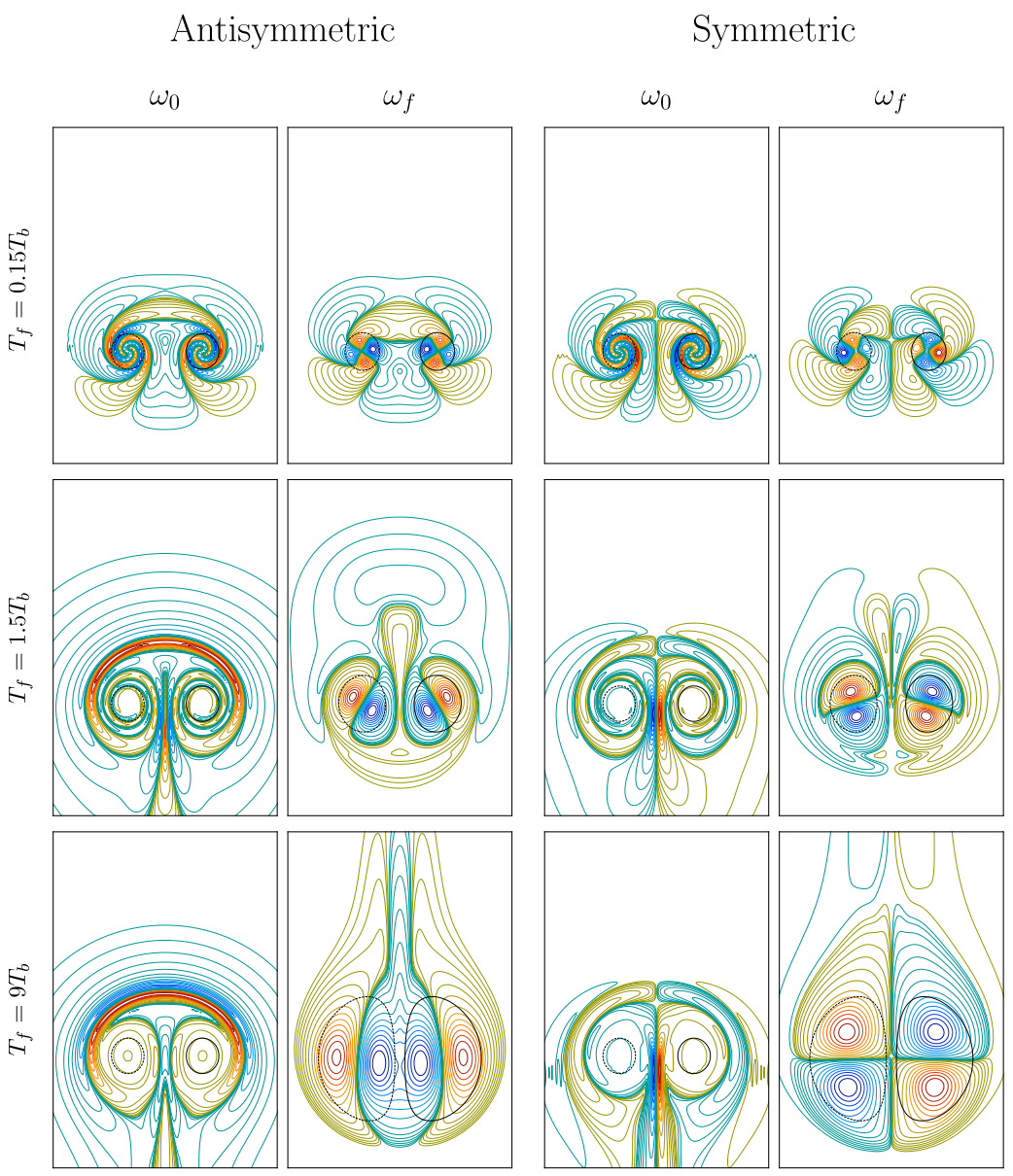

FIG. 13. Optimal perturbation ω_0 and optimal outcome ω_f vorticity fields obtained for a LOD with $(a_0/b_0, \mathrm{Re}) = (0.15, 1280)$ and three different horizon times. A small part of the computational domain is represented, i.e., $(x, y) \in [-2b, 2b] \times [-1.5b, 10b]$ and the E_3 scale is used. The solid and dotted thin lines correspond, respectively, to $\omega_B = \pm 0.1 \|\omega_B\|_\infty$.

core-contamination through velocity induction, as originally described by Antkowiak and Brancher [33]. The resemblance of the unstable modes of Sec. III with the optimal response at the horizon time indicates that such instabilities can nevertheless develop in a time evolving base flow when the structure of the initial perturbation anticipates the evolution of the base flow and takes advantage of mechanism of transient energy growth in its early development.

The structures of the optimal perturbations and associated outcomes have been also examined for different values of the aspect ratio and the Reynolds number. They do not differ from the ones described previously for $(a_0/b_0, \mathrm{Re}) = (0.15, 1280)$ and are not shown here. There is only one difference at low Reynolds numbers for the short time dynamics. For $\mathrm{Re} = 223$ and $T_f = 0.15T_b$, the optimal perturbation is structured on a $m = 1$ pattern of vorticity layers and gives rise to a displacement mode within each vortex core rather than the $m = 2$ deformation mode observed in Fig. 13.

The structure and the evolution of the optimal perturbations computed in the present work do not correspond exactly to what has been recently observed by Navrose *et al.* [32] for a LOD with $(a/b, \mathrm{Re}) = (0.18, 1000)$ [see their Fig. 20(b)]. If their optimal perturbation obtained for $T_f = 2.5T_b$ consists in similar spiraling arms of vorticity located at the periphery of the vortex centers as those illustrated in Fig. 13 for $T_f = 1.5T_b$, then their evolved state at the horizon time takes the form of a $m = 2$ deformation mode in each vortex core rather than the displacement mode observed in the present study. This optimal outcome corresponds to what has been observed here for the short time dynamics, i.e., $T_f = 0.15T_b$, and this difference in the results is not understood.

C. Transient growth on a near-field elliptical vorticity sheet

The aim of this section is to verify if the two-dimensional modes can still emerge when considering the complete history of the aircraft wake, i.e., taking into account the rolling phase of the vorticity sheet generated at the trailing edge of the wing. We consider two different configurations used by Spalart [3] and corresponding to the cruise and the high-lift takeoff or landing phases. The initial vorticity field of the base flow is obtained from the convolution of a given circulation distribution $\Gamma(x)$ with the Gaussian function $G(x, y) = \exp\left(\frac{x^2+y^2}{h_e^2}\right)$,

$$\omega_B(x, y) = \iint -\frac{d\Gamma(x - x')}{dx}\delta(y - y')\exp\left(\frac{x^2 + y^2}{h_e^2}\right)dx'dy', \tag{14}$$

where h_e measures the initial width of the vorticity sheet and δ is the Dirac function. The two circulation distributions used are an ideal elliptic distribution $\Gamma_1(x)$ for the cruise phase and a double-elliptic one $\Gamma_2(x)$ for the high-lift configuration defined, respectively, by

$$\Gamma_1(x) = \begin{cases} \Gamma_0\sqrt{1 - 4x^2/l_w^2} & \text{if} \quad |x| \leqslant l_w/2 \\ 0 & \text{if} \quad |x| > l_w/2 \end{cases} \tag{15}$$

and

$$\Gamma_2(x) = \begin{cases} \Gamma_2\sqrt{1 - 4x^2/l_{w2}^2} + \Gamma_1\sqrt{1 - 4x^2/l_{w1}^2} & \text{if} \quad |x| \leqslant l_{w2}/2 \\ \Gamma_1\sqrt{1 - 4x^2/l_{w1}^2} & \text{if} \quad l_{w2}/2 < |x| \leqslant l_{w1}/2 \\ 0 & \text{if} \quad |x| > l_{w1}/2 \end{cases}, \tag{16}$$

where $l_w = 4l_0/\pi$, $l_{w1} = 1.496l_0$, $l_{w2} = 0.6l_0$, $\Gamma_1 = 0.7514\Gamma_0$, and $\Gamma_2 = 0.2486\Gamma_0$. The wingspan denoted l_0 is used as the characteristic length scale and the initial width of the vorticity sheet is chosen arbitrarily to be $h_e = 0.05l_0$. As for the LOD, the base flow is obtained by the time integration of Eqs. (1) and (2) from the initial fields Eqs. (14)–(16) using the same pseudospectral code. The size of the domain is unchanged, i.e., $L_x \times L_y = 12b_0 \times 16b_0$, and the mesh size is kept to 2400×3200 so that $\Delta x = \Delta y \leqslant h_e/5$ and consequently $\Delta x = \Delta y \leqslant a/5$ throughout the simulation since $a \geqslant h_e$. The evolution of the vorticity sheet toward a LOD is obtained for three values of the Reynolds number, $\mathrm{Re} \in \{223, 1280, 5000\}$, and the corresponding vorticity fields are illustrated in Fig. 14 for $\mathrm{Re} = 1280$. The extrema of vorticity are initially localized at the inflection points of the circulation distributions: two for the elliptic one Eq. (15) and four for the double-elliptic one Eq. (16). The vorticity sheet progressively rolls up to give rise ultimately to a dipolar structure

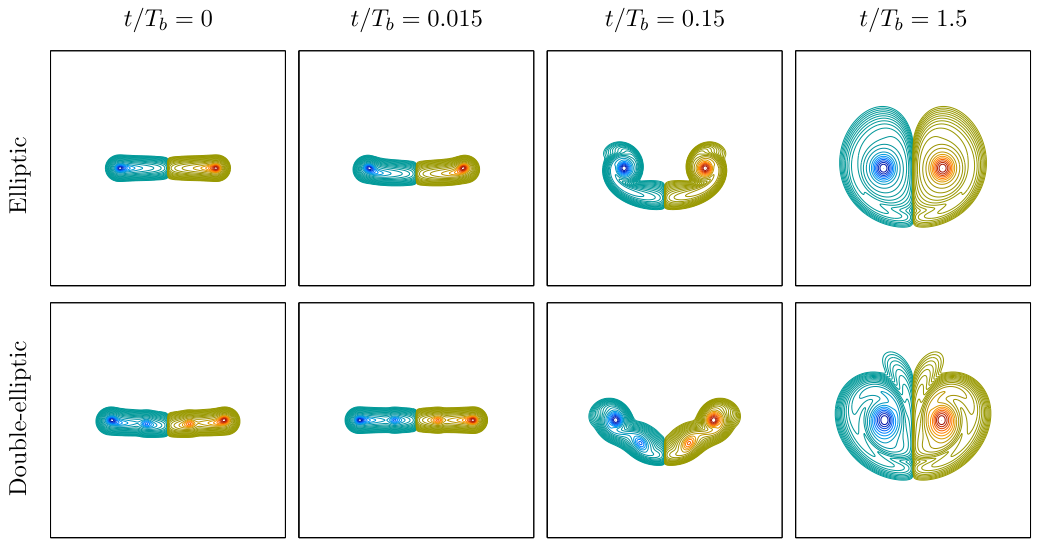

FIG. 14. Time evolution of the vorticity field (scale E_5) for an elliptic (top) and a double-elliptic (bottom) vorticity sheets at $\mathrm{Re} = 1280$. A small part of the computational domain is represented, i.e., $(x, y) \in [-1.5b, 1.5b]^2$ for $t/T_b \in \{0, 0.015, 0.15\}$ and $(x, y) \in [-2b_0, 2b_0]^2$ for $t/T_b = 1.5$.

close to one of the LOD. In the double-elliptic case, the evolution of the vorticity sheet exhibits first a quadrupolar form which converges towards the LOD through the merger of the smaller inner vortices with the outer larger ones.

As for the transient dynamics of the LOD, the optimal perturbations developing on the vorticity sheets are investigated for three different horizon times when seeded at the initial time of the base flow, which would correspond to a perturbation injected at the trailing edge of the wing. The three chosen horizon times correspond, respectively, to 1, 10, and 100 vortex core rotations: $T_f = 2\pi T_a \approx 0.015 T_b$, $T_f = 20\pi T_a \approx 0.15 T_b$, and $T_f = 200\pi T_a \approx 1.5 T_b$, where the vortex core a and the vortex separation distance b have been computed classically by $a = \sqrt{a_x^2 + a_y^2}$ and $b = 2x_c$. Figure 15 presents the energy gain evolution of these optimal perturbations for three Reynolds numbers, $\mathrm{Re} \in \{223, 1280, 5000\}$, for both the antisymmetric and the symmetric cases. The trends are similar to what has been observed for the LOD except that the levels of energy gain are much weaker, especially for the antisymmetric perturbations with a difference up to almost three orders of magnitude for the largest energy gain measured at $T_f = 1.5 T_b$ and $\mathrm{Re} = 5000$. While the energy gain increases with the horizon time and with the Reynolds number, the mean growth rate $\frac{\log G(T_f)}{2T_f}$ decreases, which indicates again that the most efficient mechanisms for energy growth operate in the short time dynamics. The perturbations grow faster in the short times, i.e., $T_f/T_b \in \{0.015, 0.15\}$, for the elliptic vorticity sheet than for the double-elliptic one. Conversely, the energy growths are larger for the double-elliptic case for the largest horizon time $T_f = 1.5 T_b$. In the case of the double-elliptic vorticity sheet, the evolution of the energy gain is not monotonous for the largest Reynolds number, i.e., $\mathrm{Re} = 5000$, which might be related to the merger of the inner vortices with the outer ones.

Figures 16 and 17 show, respectively, the vorticity field of the optimal perturbation ω_0 and optimal outcome ω_f for the elliptic and double-elliptic vorticity sheets. Both the symmetric and antisymmetric perturbations are displayed for the three selected horizon times $T_f/T_b \in \{0.015, 0.15, 1.5\}$ and a Reynolds number of $\mathrm{Re} = 1280$. At large horizon time $T_f/T_b = 1.5$, these vorticity fields are very similar to those observed for the LOD. The optimal perturbation consists of coiled vorticity layers located at the periphery of the vorticity sheet and they give rise to a displacement mode within each vortex core, which corresponds to the two-dimensional unstable mode of the dipole. The

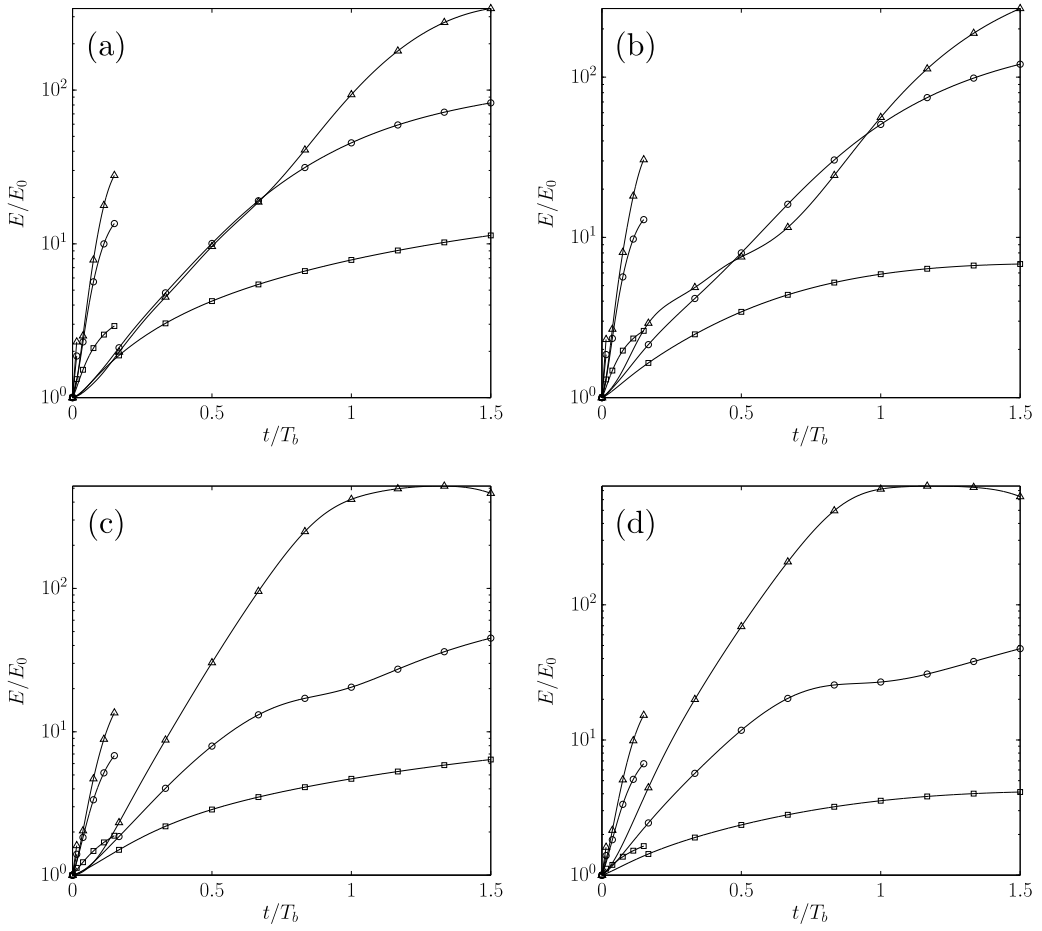

FIG. 15. Time evolution of the energy gain of the (a), (c) antisymmetric and (b), (d) symmetric optimal perturbations obtained for an elliptic (top) and a double-elliptic (bottom) vorticity sheet of initial width $h_e/l_0 = 0.05$ for three horizon times, $T_f/T_b \in \{0.05, 0.15, 1.5\}$, and three Reynolds numbers, $\mathrm{Re} = 223$ (□), $\mathrm{Re} = 1280$ (◯), and $\mathrm{Re} = 5000$ (△).

energy growth is thus associated with the same physical mechanisms combining the Orr mechanism together with a core contamination due to velocity induction. This similarity is not surprising since both the elliptic and double-elliptic vorticity sheets converge towards a LOD at large times. For the intermediate horizon time $T_f/T_b = 0.15$, the optimal response takes also the form of a displacement mode inside each vortex core but it is triggered by initial vorticity layers localized closer to, if not inside, the vorticity sheet. Finally, the short transient dynamics differs from the one of the LOD since the optimal outcome exhibits also two dipolar structures located at the outer sides of the vorticity sheet rather than the deformation Kelvin waves observed in each vortex of the LOD. Because the optimization time interval is very short, $T_f/T_b = 0.015$, the structure of the optimal perturbation is very close to the optimal response and the energy gain results only from the Orr mechanism in this case. These results allow to conclude that the rolling of the vorticity layer in the near-field of the wake does not have a significant influence on the linear development of the two-dimensional perturbations. Brion [36] drew the same conclusion for axial wave numbers corresponding to the Crow instability.

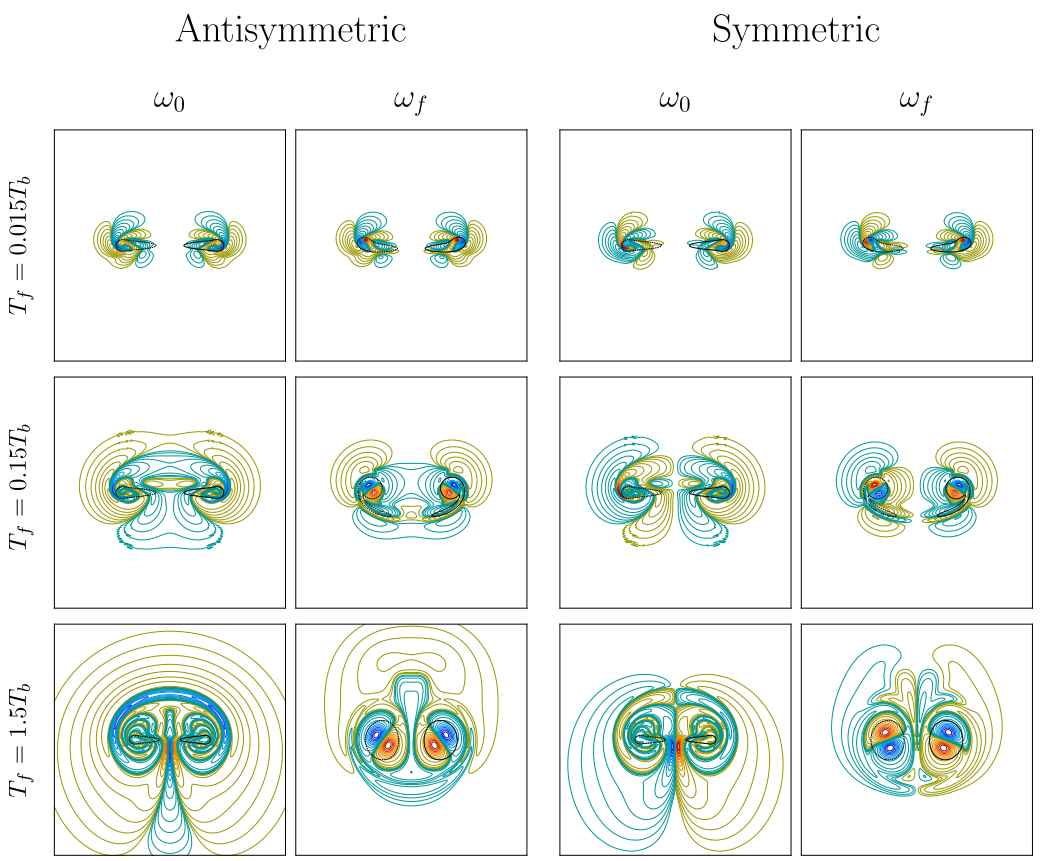

FIG. 16. Optimal perturbation ω_0 and optimal outcome ω_f vorticity fields obtained for an elliptic vorticity sheet with $(h_e, \mathrm{Re}) = (0.05, 1280)$ and three different horizon times. A small part of the computational domain is represented, i.e., $(x, y) \in [-1.5b, 1.5b]^2$ for $t/T_b \in \{0, 0.015, 0.15\}$ and $(x, y) \in [-2b_0, 2b_0]^2$ for $t/T_b = 1.5$. The E_4 scale is used. The solid and dotted thin lines correspond, respectively, to $\omega_B = \pm 0.1\|\omega_B\|_\infty$.

V. CONCLUSIONS

The two-dimensional linear dynamics of aircraft wake models has been investigated by means of modal and nonmodal stability analyses. In a first part, we extended the study of Brion *et al.* [14] who identified a new two-dimensional unstable mode thanks to a modal stability analysis performed on the Lamb-Chaplygin dipole (LCD). The present analysis was conducted for a family of viscous dipoles named Lamb-Oseen dipoles (LOD) because they are obtained numerically from the initial superposition of two counter-rotating Lamb-Oseen vortices. As shown by Sipp *et al.* [16], Delbende and Rossi [21], their characteristics depend only on the dipole aspect ratio a/b where a and b are the vortex dispersion radius and the vortex separation distance. A specific attention has been paid to the evaluation of the dipole descent velocity necessary to study the vortex pair in its own frame of reference since it has a strong influence on the unsteadiness of the dipole and consequently on the stability results. It has been shown that the velocity of the vorticity extrema is the best choice to minimize the unsteadiness of the base flow. The two-dimensional modal analysis has been conducted for the LOD family with aspect ratios in the range of $a/b \in [0.05; 0.36]$ and various Reynolds numbers. Different branches of both oscillatory and stationary unstable modes were identified, all of them consisting of two displacement modes located within the core of each vortex of the dipole, like the one observed by Brion *et al.* [14] for the LCD. Their growth rates

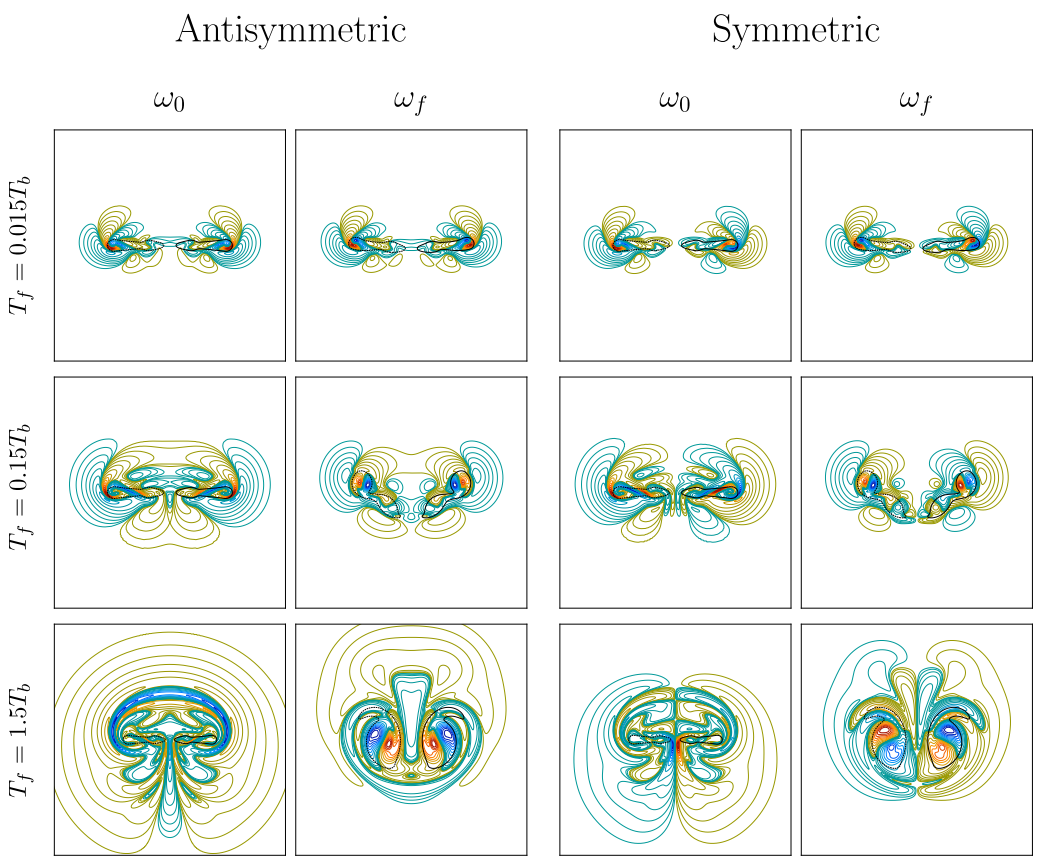

FIG. 17. Optimal perturbation ω_0 and optimal outcome ω_f vorticity fields obtained for a double-elliptic vorticity sheet with $(h_e, \mathrm{Re}) = (0.05, 1280)$ and three different horizon times. Same conventions as described in the caption of Fig. 16.

increase for decreasing Reynolds numbers indicating a non trivial destabilizing action of viscosity. These modes induce a rotation and a translation of the vortex pair which results in a zigzagging motion of the dipole. When compared to the viscous characteristic time scale $T_\nu = a_0^2/4\nu$, most of the unstable modes are not growing fast enough to survive the base flow diffusion except the antisymmetric ones occurring at large aspect ratios and large Reynolds numbers. This is confirmed by linear numerical simulations in which the base flow is allowed to evolve under viscous diffusion. The growth of two-dimensional modes is quickly stopped implying that these modes are not likely to develop.

Despite these negative conclusions, it turns out that these two-dimensional modes can nevertheless occur in LOD by taking advantage of transient growth mechanisms. This is attested by looking for the optimal perturbations thanks to a nonmodal stability analysis based on a direct-adjoint approach. The observed energy gains are substantial indicating the efficiency of transient mechanisms. In the short time dynamics, the optimal perturbation consists of intertwined vorticity layers located within each vortex core and leading to a $m = 2$ deformation Kelvin wave thanks to the Orr mechanism. For moderate to large horizon times, the optimal perturbation takes the form of vorticity layers localized outside the vortex core along the contracting manifold of the trailing (respectively, leading) hyperbolic stagnation point for the antisymmetric (respectively, symmetric) case. They eventually give rise to the two-dimensional unstable mode unveiled by the modal analysis through a combination of Orr mechanism and core contamination. We finally look at

the robustness of the modes by considering the initial stage of the development of aircraft wakes. The optimal perturbations developing on an elliptic and a double-elliptic vorticity sheet present lower but significant energy gains and they do not differ notably from the ones observed for the LOD. It indicates that the rolling of the vorticity sheet in the near-field of the wake does not have a strong influence on the linear development of the two-dimensional perturbations, a conclusion previously inferred by Brion [36] for three-dimensional perturbations with axial wave numbers corresponding to the Crow instability.

The present study confirms the existence of the two-dimensional modes of Brion *et al.* [14] in more realistic vortex dipole models and provides a convincing and positive conclusion about their possible occurrence in time-varying wake vortex models. In a three-dimensional flow, they would compete with the classic Crow and elliptic instabilities which growth rates are substantially higher than those measured here for the two-dimensional modes. Donnadieu *et al.* [18] obtained normalized growth rate of $\sigma^* = 0.73$ for the Crow instability and $\sigma^* = 0.5$ for the elliptic instability at $\mathrm{Re} = 2000$ for a LOD of aspect ratio $a/b = 0.206$, which is at least five times greater than the growth rate measured here for the antisymmetric mode for the same parameters. This difference could explain why these two-dimensional modes have never been observed experimentally so far. Besides, in real aircraft wakes, the trailing vortices exhibit a wake component associated with a non zero axial velocity. In the two-dimensional limit, this axial flow does not have any influence on the development of the instability since the equation of the axial velocity perturbation is decoupled from the equations of the two other components of the perturbation velocity. Thus, for a prescribed axial velocity of the base flow, it is possible to reconstruct directly the third component of the perturbation velocity from the two-dimensional mode corresponding to the base flow without axial flow. Consequently, the results obtained in the present study are also relevant for a vortex dipole with axial flow. Nevertheless, some extensions to this work could be performed. It would be interesting to look at the influence of the nonlinear terms on the development of these modes by performing direct numerical simulations. The effect of the stratification could be also investigated. In the three-dimensional case, Nomura *et al.* [37] and Donnadieu *et al.* [38] showed that a strong stratification ($\mathrm{Fr} \leqslant 1$) induces significant variations of both the perturbation wave number and its radial structure due to base flow modifications where the two vortices of the dipole are getting closer because of baroclinic effects.

[1] F. G. Noppel, Contrail and cirrus cloud avoidance technology, Ph.D. thesis, Cranfield University (2007).
[2] D. S. Lee, D. W. Fahey, P. M. Forster, P. J. Newton, R. C. N. Wit, L. L. Lim, B. Owen, and R. Sausen, Aviation and global climate change in the 21st Century, Atmos. Environ. **43**, 3520 (2009).
[3] P. R. Spalart, On the motion of laminar wing wakes in a stratified fluid, J. Fluid Mech. **327**, 139 (1996).
[4] P. R. Spalart, Airplane trailing vortices, Annu. Rev. Fluid Mech. **30**, 107 (1998).
[5] B. J. Bayly, Three-dimensional centrifugal-type instabilities in inviscid two-dimensional flows, Phys. Fluids **31**, 56 (1988).
[6] E. W. Mayer and K. G. Powell, Viscous and inviscid instabilities of a trailing vortex, J. Fluid Mech. **245**, 91 (1992).
[7] D. Fabre and L. Jacquin, Viscous instabilities in trailing vortices at large swirl numbers, J. Fluid Mech. **500**, 239 (2004).
[8] L. Joly, J. Fontane, and P. Chassaing, The Rayleigh-Taylor instability of two-dimensional high-density vortices, J. Fluid Mech. **537**, 415 (2005).
[9] T. Leweke, S. Le Dizès, and C. H. K. Williamson, Dynamics and instabilities of vortex pairs, Annu. Rev. Fluid Mech. **48**, 507 (2016).
[10] S. C. Crow, Stability theory for a pair of trailing vortices, AIAA J. **8**, 2172 (1970).
[11] S. E. Widnall, D. B. Bliss, and C.-Y. Tsai, The instability of short waves on a vortex ring, J. Fluid Mech. **66**, 35 (1974).

[12] D. W. Moore and P. G. Saffman, The instability of a straight vortex filament in a strain field, Proc. R. Soc. London A **346**, 413 (1975).
[13] C.-Y. Tsai and S. E. Widnall, The stability of short waves on a straight vortex filament in a weak externally imposed strain field, J. Fluid Mech. **73**, 721 (1976).
[14] V. Brion, D. Sipp, and L. Jacquin, Linear dynamics of the Lamb-Chaplygin dipole in the two-dimensional limit, Phys. Fluids **26**, 064103 (2014).
[15] P. Billant, P. Brancher, and J.-M. Chomaz, Three-dimensional stability of a vortex pair, Phys. Fluids **11**, 2069 (1999).
[16] D. Sipp, L. Jacquin, and C. Cosssu, Self-adaptation and viscous selection in concentrated two-dimensional vortex dipoles, Phys. Fluids **12**, 245 (2000).
[17] S. Le Dizès and F. Laporte, Theoretical predictions for the elliptical instability in a two-vortex flow, J. Fluid Mech. **471**, 169 (2002).
[18] C. Donnadieu, S. Ortiz, J.-M. Chomaz, and P. Billant, Three-dimensional instabilities and transient growth of a counter-rotating vortex pair, Phys. Fluids **21**, 094102 (2009).
[19] J. D. Crouch, Instability and transient growth for two trailing-vortex pairs, J. Fluid Mech. **350**, 311 (1997).
[20] D. Fabre and L. Jacquin, Stability of a four-vortex aircraft wake model, Phys. Fluids **12**, 2438 (2000).
[21] I. Delbende and M. Rossi, The dynamics of a viscous vortex dipole, Phys. Fluids **21**, 073605 (2009).
[22] L. Jacquin, D. Fabre, P. Geffroy, and E. Coustols, The properties of a transport aircraft wake in the extended nearfield: An experimental study, in *39th AIAA Aerospace Sciences Meeting and Exhibit*, AIAA Paper 2001-1038 (AIAA, 2001).
[23] Ömer Savaş, Experimental investigations on wake vortices and their alleviation, C. R. Phys. **6**, 415 (2005).
[24] W. J. Devenport, M. C. Rife, S. I. Liapis, and G. J. Follin, The structure and development of a wing-tip vortex, J. Fluid Mech. **312**, 67 (1996).
[25] C. Donnadieu, Dynamique des sillages tourbillonnaires en milieu homogène et stratifié, Ph.D. thesis, École Polytechnique, Paris (2008).
[26] R. Jugier, Stabilité bidimensionnelle de modèles de sillage d'aéronefs, Ph.D. thesis, ISAE, Université de Toulouse (2016).
[27] D. Sipp, F. Coppens, and L. Jacquin, Theoretical and numerical analysis of wake vortices, ESAIM: Proc. **7**, 397 (1999).
[28] Note that they mention a value of $\mathrm{Re} = 22$ in their paper which has been corrected using the present definition of the Reynolds number $\mathrm{Re} = \Gamma/\nu$ instead of $\mathrm{Re} = UD/\nu$, with the relation $UD \approx 0.2928\Gamma$.
[29] Note that they mention a value of $a/b \approx 0.448$ for the aspect ratio of the LCD, which is slightly higher than the one used in the present study. The difference comes from the evaluation of the vortex centers which is given here by the position of the vorticity extrema rather than the first order vorticity momentum.
[30] D. Fabre, D. Sipp, and L. Jacquin, Kelvin waves and the singular modes of the Lamb-Oseen vortex, J. Fluid Mech. **551**, 235 (2006).
[31] D. C. Hill, Adjoint systems and their role in the receptivity problem for boundary layers, J. Fluid Mech. **292**, 183 (1995).
[32] Navrose, H. G. Johnson, V. Brion, L. Jacquin, and J. C. Robinet, Optimal perturbation for two-dimensional vortex systems: route to non-axisymmetric state, J. Fluid Mech. **855**, 922 (2018).
[33] A. Antkowiak and P. Brancher, Transient energy growth for the Lamb-Oseen vortex, Phys. Fluids **16**, L1 (2004).
[34] J. Fontane, P. Brancher, and D. Fabre, Stochastic forcing of the Lamb-Oseen vortex, J. Fluid Mech. **613**, 233 (2008).
[35] V. Brion, D. Sipp, and L. Jacquin, Optimal amplification of the Crow instability, Phys. Fluids **19**, 111703 (2007).
[36] V. Brion, Stabilité des paires de tourbillons contra-rotatifs: application au tourbillon de jeu dans les turbomachines, Ph.D. thesis, École Polytechnique, Paris (2009).
[37] K. K. Nomura, H. Tsutsui, D. Mahoney, and J. W. Rottman, Short-wavelength instability and decay of a vortex pair in a stratified fluid, J. Fluid Mech. **553**, 283 (2006).
[38] C. Donnadieu, S. Ortiz, and J.-M. Chomaz, Three-dimensional instabilities and optimal perturbations of a counter-rotating vortex pair in stratified flows, Phys. Fluids **27**, 106603 (2015).